วารสารวิศวกรรมศาสตร์และนวัตกรรม
Journal of Engineering and Innovation

บทความวิจัย

Elasto-plastic deformation analysis of A1050P aluminum sheet subjected to three-point bending and estimation of the springback of the bent sheet

Weerayut Jina*[1] Sungkom Srisomporn[1] Rungtawee Padakan[1] Arthit Sangngam[1] Patchara Wongthong[2] Montri Sangsuriyun[3]

[1] Department of Mechanical and Manufacturing Engineering, Kasetsart University, Chalermphrakiat Sakon Nakhon Province Campus, Sakon Nakhon 47000

[2] Faculty of Engineering, Bangkokthonburi University, Bangkok, 10170

[3] Department of Industrial Engineering, Nakhon Phanom University, Nakhon Phanom 48000

* Corresponding author.

E-mail: weerayutjina@gmail.com, weerayut.j@ku.th (W. Jina); Telephone: 0 91858 4719

Received 3 March 2024; Revised #1 25 May 2024; Accepted 16 July 2024

Abstract

This study describes thethree-point bending deformation characteristics of the bent partof an aluminum alloy sheet(A1050P). The elasto-plastic states in the bent zone of the worksheet at bending angles of 0°–90° were simulated using the finite element method (FEM). To develop a simulation bending model, a three-point bending experiment was conducted using a 0.39-mm-thick aluminum sheet. The bending load resistance and deformation profile of the bent part in the FEM model were compared with the experimental results, and the initial punch indentation depth (d_P) was varied within a certain range. The FEM modelwas developed and simulated using isotropic elasto-plastic solid properties. When simulating the three-point bending process, the modification of the plastic coefficient appears to be the primary characteristic that closely matches the experimental results. Through the FEM simulation of the worksheet, the following results were obtained: (1) The contract friction force (μ_c) between the worksheet and the channel die was greater than that between the punch and the worksheet. This may be due to the boundary conditions of the three-point bending apparatus. (2) The pressure dependency of the friction coefficient is important. Further investigation into this pressure dependency, specifically the relationship between contact pressure and frictional resistance, should be considered. (3) The corner radius of the channel dies had a greater impact on the maximum principal compressive stress (σ_{P2max}) than the maximum principal tensile stress (σ_{P1max}), primarily because of the abrasive forces encountered during the three-point bending process. The peak maximum ratio of σ_{P2max} by σ_{P1max} was approximately 1.12–1.27. An appropriate round edge of the corner die is important. (4) The number of nonlinear elasto-plastic states at the bending zone appeared to be three. The different separations in the three states may be due to the three different stress distribution patterns. (5) Regarding springback, for large (deep) deformations, Gardiner's model closely matched the simulation model. This was confirmed by comparing the undefined V-notch with the applied V-notch. However, for small (shallow) deformations, further investigation is required through experimentations.

Keywords

finite element method; three-point bending test; aluminum sheet A1050P; nonlinear elasto-plastic states

1. Introduction

The aluminum alloy sheet A1050P is extensively used in semiconductor packages because of its beneficial characteristics, including its low price, high strength, high plasticity, good formability, lightweight material, electrical conductivity, corrosion resistance, and good thermal conductivity. The three-point bending test is one of the most important material testing methods for determining the mechanical performance of materials during the manufacturing process. The bending method has recently been discovered to bend any shape of precision parts, such as lead frames for LSI chips and integrated circuits.

One of the most important steps in the bending process is to estimate the bending deflection, bending strength, bending fatigue, sheet thickness, sheet setting condition, die angle, die opening, and punch radius [1-3]. Furthermore, the springback effect was studied. [4-14]. The influence of the punch tip radius and bending angle on the spring-forward behavior of Al–Mg–Si alloys during the V-bending process was investigated [4]. The springback phenomena associated with metal sheets during deformation have been studied using V-die punches with appropriate dimensions [5]. The three-point bending test, including the springback stage, was systematically examined through numerical simulations. For comparison, two elasto-plastic constitutive models were introduced in the finite element code [6]. A newly proposed elasto-plastic constitutive model was used that considers initial and induced anisotropies, combined nonlinear isotropic and kinematic hardenings, and isotropic ductile damage. To examine the springback phenomena in nonproportional strain paths, three-point bending tests were conducted [7]. The validation of Gardiner's theoretical model was compared with the simulated springback responses [8]. The effectiveness of using a tip-bottomed punch to reduce springback in ultra-high-strength steel was investigated [9]. The springback problem in sheet metal press-brake air bending aims to predict the punch displacement required to achieve the desired bending angle [10]. The vertical displacements and springback factors, along with the total equivalent plastic strain and equivalent von Mises stress, were also presented [11]. The tool path geometry and friction-induced effects on sheet materials were employed to reduce springback, and the optimization of the sheet metal bending process was examined [12]. The decrease in the amount of springback with increasing plate thickness was also investigated [13]. The double-bend technique effectively reduced springback [14].

The effects of different hardening models, such as isotropic, kinematic, and combined hardening rules, on various uncoupled ductile fracture criteria were explored using both experimental and numerical methods [15]. The effects of plate thickness and punch radius were investigated [16-17]. The effects of the friction coefficient on tension and compression stresses were investigated [16]. The elasto-plastic behavior of aluminum sheets was simulated under nonlinear conditions [18].

Several studies have experimentally and numerically investigated the three-point bending test of aluminum sheets [7-8,19-21]. The mechanical behavior of the material on various strain paths, including tension in straight and notched samples and equi-biaxial tension, was examined up to the point of necking and final rupture [19]. The effects of roll distance and crack initiation on the bending curve shape were investigated [20]. The bending process of specimens with various punch radii in a three-point bending test was investigated [21].

Numerous studies have investigated the formation process of the aluminum alloy sheet A1050P. The effects of the thickness of aluminum sheets and friction on the load characteristics of a crushed center bevel cutter indented onto an aluminum sheet were previously explained [22]. The relationship between the thickness of the wedged sheet and the tip thickness of the crushed cutter was also investigated [23]. The critical conditions for cutting aluminum sheets were investigated [24]. The sensitivity of crack propagation in an aluminum worksheet during wedge shearing was studied [25]. The impacts of various rolling parameters on the void volume fraction and void shape in aluminum were investigated [26]. The dislocation density at the mid-thickness of an aluminum alloy was estimated [27]. A feasibility study was conducted to investigate the friction coefficient between tools and aluminum sheets and to analyze the maximum principal tensile and compressive stresses [28].

However, to date, the deformation of nonlinear elasto-plastic states at the center of the bent zone of the aluminum alloy sheet A1050P has not been reported. Therefore, in this study, the simulation bending model was compared with the experimental results to verify the bending load resistance and deformation profile of the worksheet. Here, the simulation model was analyzed at bending angles of 0°–90°, which corresponded to a punch indentation depth d_P = 0–2.0 mm. In addition, the σ_{P1max} (maximum principal tensile stress) and the σ_{P2max} (maximum principal compressive stress) were estimated via finite element method (FEM) simulation. The springback effect on the worksheet (nonmodified shape versus the modified shape such as a V-notch) was considered in the FEM simulation. Finally, the simulation model was validated using Gardiner's model.

Table 1 In-plane tensile properties of aluminum sheet (A1050P) [25,28] and mechanical conditions of aluminum sheet for simulation model.

In-plane tensile properties of A1050P	
Thickness t [mm]	0.39
Young's modulus E [GPa]	78.6
Yield Stress σ_Y [MPa]	140
Ultimate tensile strength σ_B [MPa]	150
Plastic coefficient, F [MPa]	90
Work hardening exponent, n	0.46
Mechanical conditions of aluminum sheet for simulation model	
Worksheet thickness t [mm]	0.39
Young's modulus E [GPa]	78.6
Poisson's ratio	0.2
Yield Stress σ_Y [MPa]	140
Ultimate tensile strength σ_B [MPa]	150
Plastic coefficient, F [MPa]	170
Work hardening exponent, n	0.46
Friction coefficients, μ_{dt}	0.2
Span length of the dies S_L [mm]	4

μ_{dt} denotes the friction coefficient between the deformable body and tools (punch and dies).

2. Materials and experimental methods

2.1 Materials

In the three-point bending experiment, a commercially pure aluminum alloy sheet (JIS-A1050P) with a thickness of 0.39 mm was used [25]. The tensile properties of the aluminum sheet in the transverse direction are shown in Table 1. The work hardening characteristics related to the stress–strain of the material were approximated by the power law expression $\sigma = F\varepsilon^n$, where F represents the plastic

coefficient, ε, denotes the equivalent plastic strain, and n represents the work hardening exponent. In this study, we mainly discuss the cross- direction of material behavior.

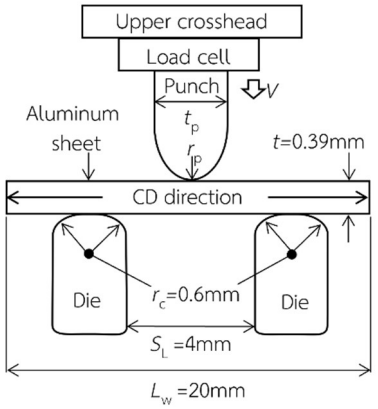

Fig. 1 Schematic of the experimental apparatus used in three-point bending tests [28].

2.2 Experimental method

To validate the simulation results, out- of- plane three- point bending experiments were conducted following the standard test (based on ASTM- D790- 3, 2003) [29], as shown in Fig. 1. The specimens were prepared as five square sheets, each with a length of L_W = 20 mm (longitudinal direction), a width of W_S = 20 mm (transverse direction), and a thickness of t = 0.39 mm. The span length of die S_L was 4 mm, and the corner radii r_c of both sides were 0.6 mm. The punch thickness t_p was 1.9 mm, and the punch radius r_p was 0. 95 mm. The upper crosshead had a punch/ indenter mounted on a load cell. The aluminum sheet was placed on the die on both sides. The punch indentation depth d_P moved downward with a velocity V = 0.1 mm·s^{-1}. The punch direction angle □ was set to 90° with respect to the cross-direction of the worksheet, as shown in Fig. 2. The bending force b_f and d_P were automatically measured using a load cell and linear gauge sensor. The specimen, both sides of the die, and the tool surface were washed with alcohol before the three- point bending test. The specimens were tested five times. The deformation profile of the bending part was observed by a charge- coupled device camera during the bending of the aluminum sheet.

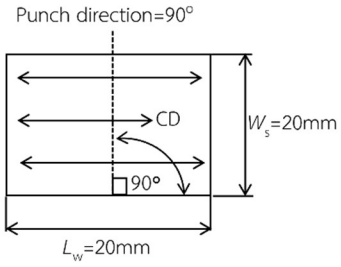

Fig. 2 Punch direction of specimen [28].

3. FEM simulation analysis of three-point bending process

The FEM simulation model accounts for the experimental observations explained in the previous section and estimates the behavior of the three-point bending mechanism in the bending stage of an aluminum sheet (JIS-A1050P). The simulation model was applied. The following actions were performed and discussed: (1) The FEM simulation models were compared with the experimental results described in Section 2.2 for a punch indentation depth d_P = 0– 2 mm. The plastic coefficient is listed in Table 1. The modification of the plastic coefficient was compared with the experimental result. The contract friction force μ_c of the worksheet and tools was investigated. (2) The friction force between the worksheet and tools was investigated. (3) The σ_{P1max} (maximum principal tensile stress) and the σ_{P2max} (maximum principal compressive stress) were examined. (4) The nonlinear elasto- plastic states were investigated in the center zone. (5) To reduce the springback, the V-notch shape was compared with the nonmodified

shape. (6) The simulation model was validated by comparing its springback ratio with that predicted by the theoretical model (Gardiner's model).

3.1 FEM simulation method in three- point bending process

The general- purpose finite element code MSC. MARC was used to simulate the three- point bending process. The updated Lagrange method and a large strain state were used to analyze a two-dimensional model (plane strain) . The Newton–Raphson method was used to solve the nonlinear equilibrium equations in the structural analysis of the worksheet [30] . Fig. 3 shows the FEM model of the bending stage based on the experimental bending stage (Section 2. 2) . The simulation model was the same as the experiment model, as illustrated in Fig. 1. The worksheet was considered a square deformable body with a length of deformable body L_d = 20 mm and a thickness of t = 0.39 mm. The four-node plain- strain quadrilateral element was used to model the worksheet. An isotropic elasto- plastic model was used to simulate the bending process using the in- plane tensile testing properties in the cross- direction [25] . The mesh model comprised a full model. A mesh independence study on the simulation model was conducted in three cases: In the case of coarse mesh (i) , the total number of elements in the worksheet was 1,170, and the total number of nodes was 1,410. In the case of medium mesh (ii) , the total number of elements in the worksheet was 5,850, and the total number of nodes was 6,510. In the case of fine mesh (iii) , the total number of elements in the worksheet was 11,700, and the total number of nodes was 12,688. Therefore, the ratio of fine to medium mesh was approximately 2, and the ratio of medium to coarse mesh was approximately 5.

In all cases, the deformable body of the worksheet was presumed to be an isotropic, elasto-plastic material conforming to the isotropic hardening power law $\sigma = F\varepsilon^n$. The plastic coefficient F = 90 MPa [25] (based on Table 1), the modification of the plastic coefficient F = 170 MPa (1.89 times F = 90 MPa from Table 1), and n = 0.46 were selected, as described in Section 2. 1. In the simulation model, all elements were assumed to have no fracture or crack during the bending process. Therefore, the Coulomb friction model was assumed for each contact surface, and the friction coefficients between the deformable body and punch- dies μ_{dt} were initially assumed to be 0. 2 [25]. The punch and dies were defined as rigid bodies. The upper punch was moved downward, while both sides of the lower dies were fixed on the vertical and horizontal axes (x, y- axis) . To prevent any tangential slip between the worksheet and tools (punch and dies) during the simulation, the worksheet was fixed on the horizontal axis (x-axis), as shown in Fig. 3. Each punch step was appropriately performed with 200 total increments to simulate the bending process during the three- point bending simulation. The simulation model was completed with a successful exit number of 3,004. There were 228 (coarse mesh), 261 (medium mesh) , and 319 (fine mesh) Newton–Raphson iteration cycles; 15 (coarse mesh) , 46 (medium mesh) , and 84 (fine mesh) contact separations; 0 cutbacks; no remesh; an analysis time of 20 s for each mesh type; compute wall times of 80 (coarse mesh) , 378 (medium mesh) , and 713 (fine mesh) . These statistics were cumulative for all load cases.

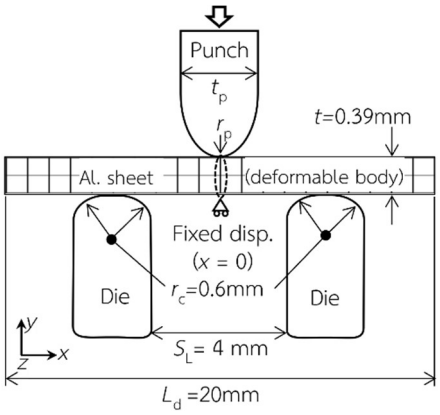

Fig. 3 Schematic of bending process for simulation model [28].

4. Results and discussions

4.1 Experimental results of three-point bending process

Fig. 4 shows the relationship between the bending force b_F and the punch indentation depth d_P. The bending force response was recorded at d_P = 0–2 mm. Here, the bending force b_F tends to increase with the punch indentation depth d_P. The linear elastic zone for the deflection of the worksheet was detected in the early stage at d_P = 0–0.14 mm. Conversely, the plastic deformation zone was detected in the range of 0.14 < d_P < 2.0 mm. Figs. 5 (a) – (e) show the representative side-view photographs of the normal bending specimens during the three-point bending test with respect to d_P values of 0, 0.5, 1, 1.5, and 2 mm. Fig. 6 shows the effect of the generated kinetic friction force at the interface between the worksheet and channel die in the three-point bending test at d_P = 0–2 mm. The worksheet was abrasive by the channel die in the three-point bending test, and the surface between the punch and worksheet was not investigated in the experiment because digital microscopes are difficult to record with. Therefore, to compare the contract friction force μ_c and punch indentation depth d_P with the simulation results, the kinetic friction forces between the worksheet and tools (punch and worksheet; channel die and worksheet) were demonstrated.

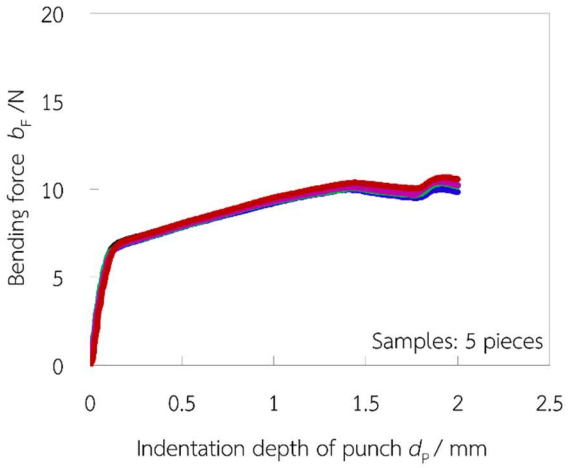

Fig. 4 Relationship between bending force bF and punch indentation depth dP in experiment for dP = 0–2 mm [28].

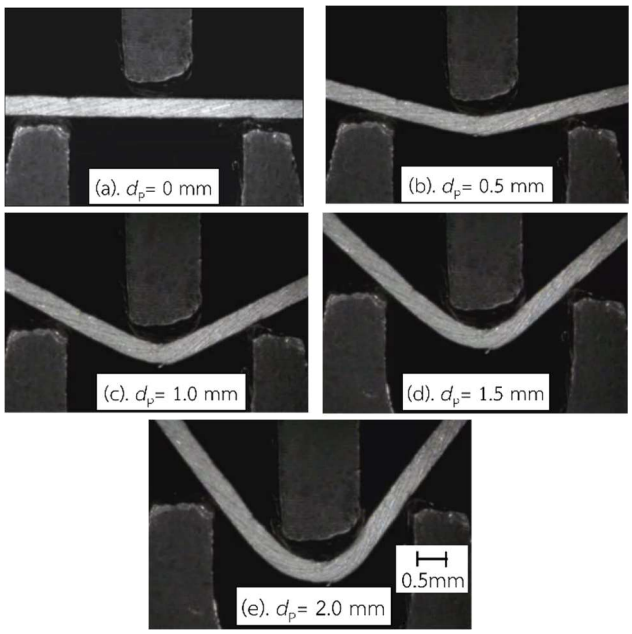

Fig. 5 Representative side views of bending deformation profile in three-point bending test at punch indentation depths dP= 0 [28], 0.5, 1 [28], 1.5 and 2 mm [28].

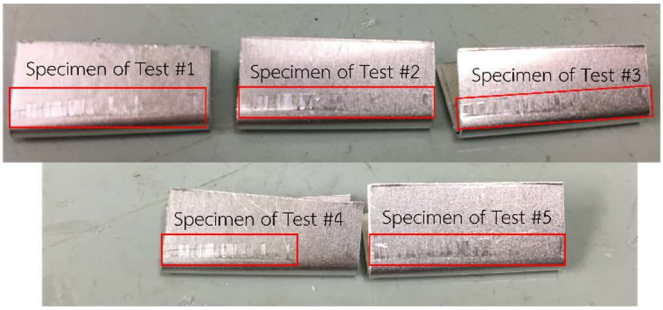

Fig. 6 Effect of abrasive zone between worksheet and channel die during three-point bending test at dP = 0–2 mm

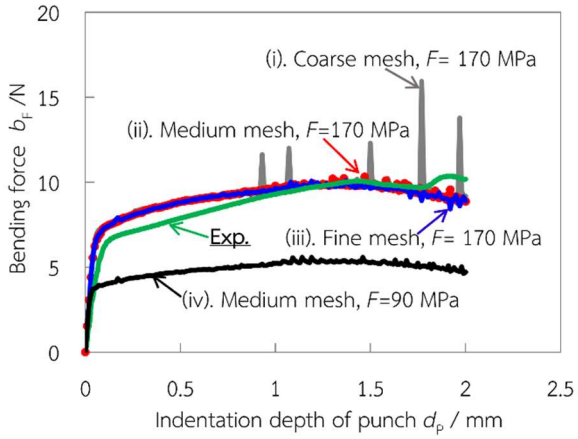

Fig. 7 Relationship between bending force bF and punch indentation depth dP in three- point bending process (comparison of simulation results with experimental results) for dP = 0–2 mm. (i) For coarse mesh, the material properties are based on the data presented in Table 1 (with the modification of plastic coefficient F = 170 MPa). (ii) For medium mesh, the material properties are based on the data presented in Table 1 (with the modification of plastic coefficient F = 170 MPa). (iii) For fine mesh, the material properties are based on the data presented in Table 1 (with the modification of plastic coefficient F = 170 MPa). (iv) For medium mesh, the material properties are based on the data presented in Table 1 (without modification of plastic coefficient F = 90 MPa) [25].

4.2 Bending load response of aluminum sheet in simulation model versus experimental results

As described in Section 3.1, the simulation results were compared to the experimental results (Fig. 7). Fig. 7 shows the relationship between the bending force b_F and the punch indentation depth d_P of the aluminum sheet. The experimental results are presented in Fig. 4. Regarding the mesh independence study, the cases of medium mesh (ii) and fine mesh (iii) fairly matched the experimental results, with small variations for $d_p < 1.0$ mm. However, the coarse mesh (i) exhibited significant fluctuations for $d_p > 0.9$ mm. To reduce the computation time, the medium mesh was used to analyze the simulation results.

Consequently, for the modified plastic coefficient F = 170 MPa, the simulation results relatively matched the experimental results. Conversely, for the nonmodification of plastic coefficient F = 90 MPa, as shown in Fig. 7 (iv), the simulation results did not match the experimental results. Therefore, based on the power law expression $\sigma = F\varepsilon^n$, a factor of 1.89 times F = 90 MPa (Table 1) was significant in confirming the experimental results.

4.3 Evaluation of kinetic friction force in worksheet under bending state

As mentioned in Section 4.1, the simulation results are presented in Fig. 8. The kinetic friction forces of the worksheet and tools (punch and worksheet; channel die and worksheet) were compared. The contract friction force μ_c was derived from the equation $P = \mu_{dt} \cdot W_s$, where P represents the pressure force, μ_{dt} denotes the friction coefficient between the deformable body and tools, and W_s denotes the width of the specimen. Consequently, the contract friction force μ_c between the channel die and worksheet tends to increase as d_P increases, whereas the μ_c between the punch and worksheet is almost independent of d_P. This result indicates that

the simulation results of μ_c between the channel die and worksheet agree with the experimental result, as shown in Fig. 6. In other words, an abrasive contact area formed between the channel die and the worksheet. When the μ_c between the punch and worksheet increased slightly, $\mu_{c(Peak)}$ was approximately 0.16. In contrast, when the μ_c between the channel die and worksheet increased for 0.05 < d_P ≤ 2.0 mm, $\mu_{c(Peak)}$ was approximately 1.03.

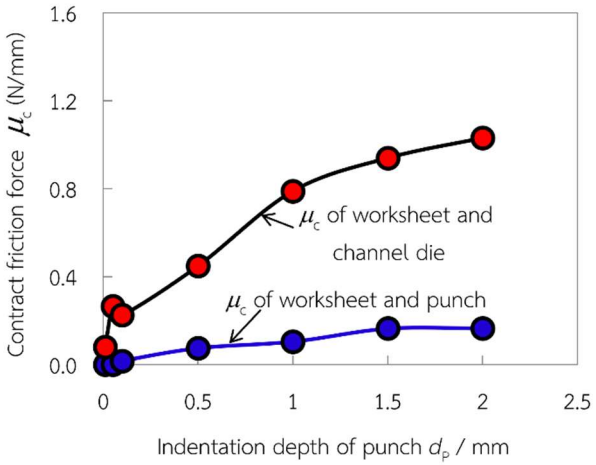

Fig. 8 Relationship between contract friction force □$_c$ and punch indentation depth dP for worksheet and tools (punch and worksheet; channel die and worksheet) in the simulation results of three-point bending process for dP = 0–2 mm.

4.4 Simulated bending profile and deformation characteristics of bending zone

Figs. 9 (a)– (e) show sectional views of the matching profile between the simulation results as contour band diagrams (first principal tensile stress σ_{P1}) versus the experimental results for d_P = 0.01–2.0 mm. The simulation results relatively matched the experimental results. Consequently, the gray band (σ_{P1} > σ_Y = 140 MPa) along the center of the bent zone in Figs. 9 (b)–(e) indicates a high-tensile state, except in Fig. 9 (a) at d_P = 0.01 mm. According to these figures, the high-tensile state seems to occur in a bent zone at d_P > 0.01 mm and appears to be slightly expanded in the lateral direction when d_P increases from 0.02 to 2.0 mm.

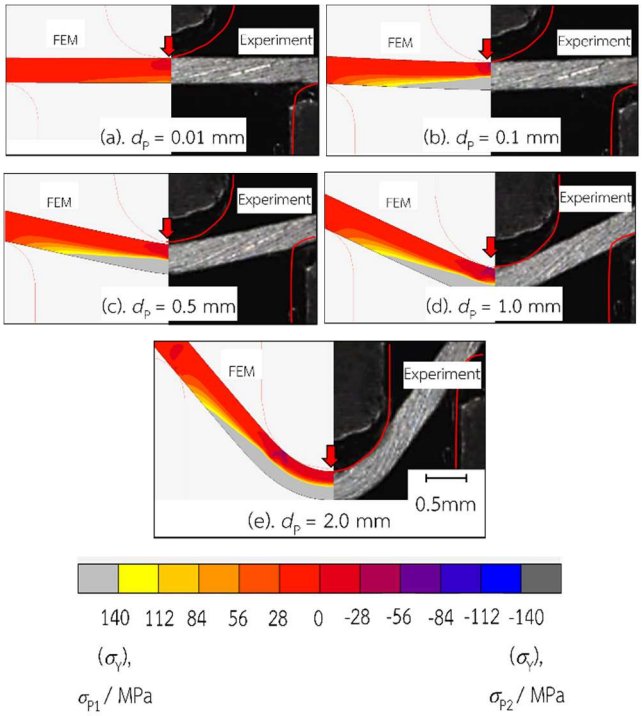

Fig. 9 Representative side views of bending deformation profile in three-point bending process for punch indentation depths d_P of (a) d_P = 0.01 mm, (b) d_P = 0.1 mm, (c) d_P = 0.5 mm, (d) d_P = 1.0 mm, and (e) d_P = 2.0 mm. The matched profile between the simulation results (left) and the experimental results (right) for the first principal tensile stress σ_{P1}

Fig. 10 shows the relationship between the bending angle B_A and the punch indentation depth d_P. The simulation and experimental results exhibited similar tendencies.

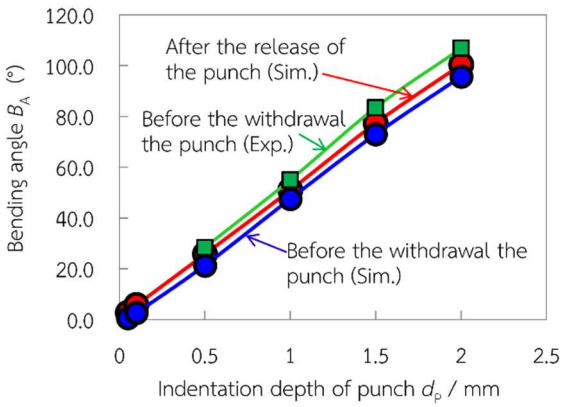

Fig. 10 Relationship between bending angle BA and punch indentation depth dP. The simulation results (based on before the withdrawal of the punch and after the release of the tool) versus the experimental results for the dP states

Fig. 11 shows representative side views of the contour band diagrams for d_P = 1.0 and 2.0 mm. From this figure, the following characteristics were revealed: (1) A high-tensile/compressive state, indicated by the light-gray and gray bands (σ_{P1} and σ_{P2} > ±140 MPa), was observed along the center of the bent zone. (2) The stress distribution on the compressive state zone of the contact body (punch versus worksheet and die versus worksheet), indicated by the dark blue and light-blue bands (σ_{P2} > −84, −112 MPa), as shown in Fig. 11, appeared to be located at the corner die and punch. The compressed state of the worksheet and die was greater than that of the worksheet and punch.

Fig. 12 shows the norms of σ_{P1max} (maximum principal tensile stress) and σ_{P2max} (maximum principal compressive stress) at the bending positions at d_P = 0.01–2.0 mm. The σ_{P1max} and σ_{P2max} of each d_P were measured in the surface layer by the simulation. The representative norms of σ_{P1max} and σ_{P2max} are represented by different colors. For the simulation results, the red line indicates $\sigma_{P1max,}$ and the blue line indicates σ_{P2max}. Consequently, they were classified into two stages: in the first stage, σ_{P1max} and σ_{P2max} significantly increased for d_P < 0.1 mm, whereas, in the second stage, σ_{P1max} and σ_{P2max} slightly increased for 0.1 < d_P ≤ 2.0 mm. However, a comparison of σ_{P1max} and σ_{P2max} showed that σ_{P2max} was significantly higher than σ_{P1max} for 0.01 ≤ d_P ≤ 2.0 mm. The ratio of σ_{P2max} by σ_{P1max} for 0.01 < d_P ≤ 2.0 mm was approximately 1.12– 1.27, primarily due to the strain restriction on the inner side of the bent body, as depicted in the representative cases of d_P = 1.0 and 2.0 mm in Fig. 11. According to the simulation results presented in Fig. 12, the peak maximum of σ_{P1max} was 288 MPa at d_P = 1.0 mm, whereas the peak maximum of σ_{P2max} was 323 MPa at d_P = 1.0 mm.

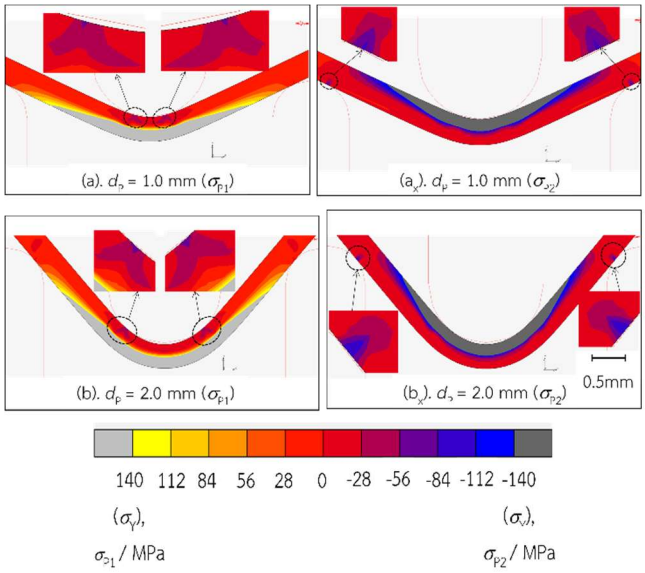

Fig. 11 Representative side views of contour band diagram of bending deformation profile in three-point bending process when comparing σ_{P1} (first principal tensile stress) and σ_{P2} (second principal compressive stress) for punch indentation depths d_P of (a) d_P = 1.0 mm (σ_{P1}), (a$_x$) d_P = 1.0 mm (σ_{P2}), (b) d_P = 2.0 mm (σ_{P1}), and (b$_x$) d_P = 2.0 mm (σ_{P2}). Figs. 11 (a) and (b) were copied from Figs. 9 (d) and (e).

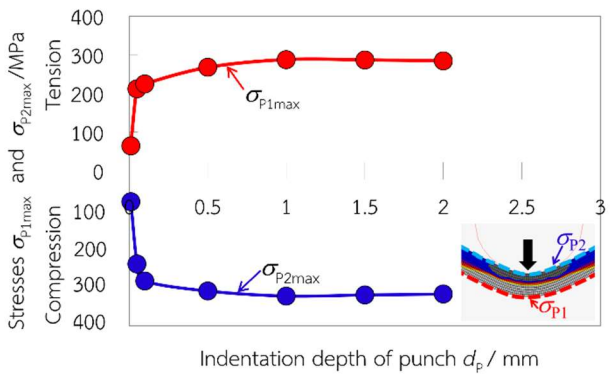

Fig. 12 Magnitude of σ_{P1max} and σ_{P2max} principal stress on worksheet surfaces (d_P = 0.01–2.0 mm)

Figs. 13 (a)–(e) show contour band diagrams with the magnitude of the equivalent stress at the bending zone during the bending process of the worksheet when observing the elasto-plastic state of the first state (shallow indentation cases, d_P = 0.08–0.12 mm). The elastic deformation at the center tends to decrease as d_P increases. Similarly, the elastic deformation was separated for 0.12 ≤ d_P ≤ 0.41 mm, as shown in Figs. 13 (e) and Fig. 14 (a).

Figs. 14 (a)–(e) show contour band diagrams with the magnitude of the equivalent stress at the bending zone during the bending process of the worksheet when observing the elasto-plastic state of the second state (intermediate indentation cases, d_P = 0.41–0.49 mm) . Consequently, the recovered elastic deformation at the center tends to increase for 0.41 < d_P ≤ 0.57 mm.

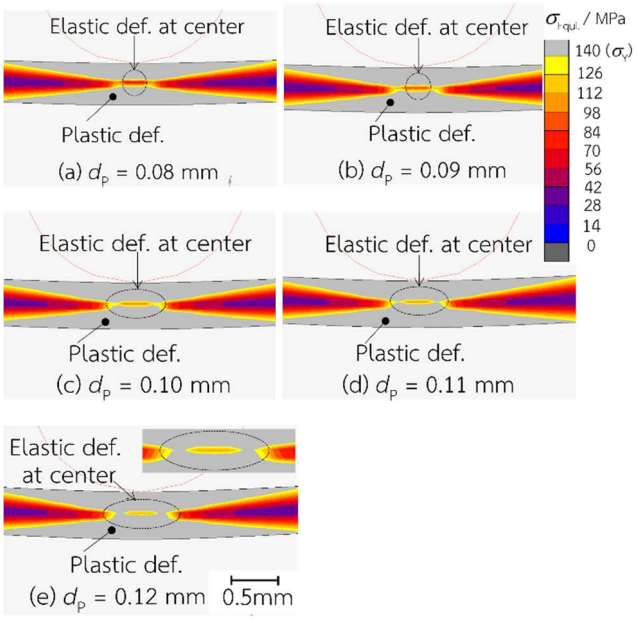

Fig. 13 Contour band diagram of equivalent stress at bending zone during the bending process of worksheet when observing elasto-plastic state (1st state). The bending profiles of the simulation results at (a) d_P = 0.08, (b) d_P = 0.09, (c) d_P = 0.10, (d) d_P = 0.11, and (e) d_P = 0.12 mm.

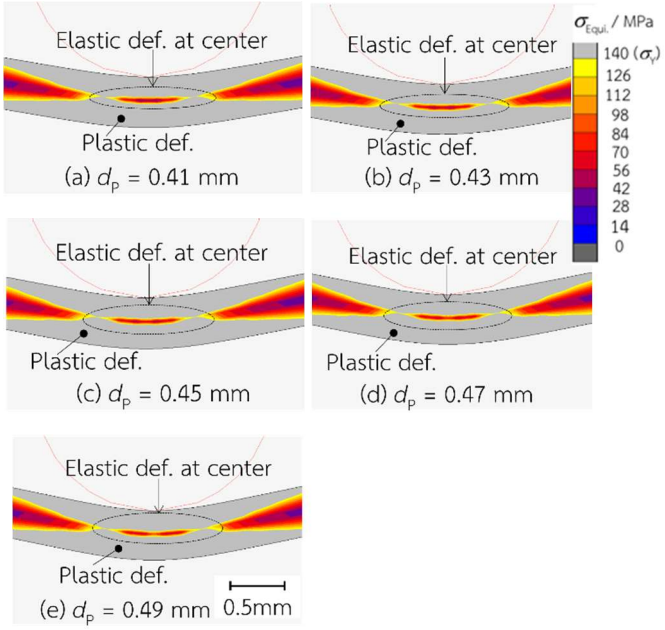

Fig. 14 Contour band diagram of equivalent stress at bending zone during the bending process of worksheet when observing the elasto-plastic state (second state). The bending profiles of the simulation results at (a) d_P = 0.41, (b) d_P = 0.43, (c) d_P = 0.45, (d) d_P = 0.47, and (e) d_P = 0.49 mm.

Figs. 15 (a)–(e) show contour band diagrams with the magnitude of the equivalent stress at the bending zone during the bending process of the worksheet when observing the elasto-plastic state of the third state (deep indentation cases, d_P = 0.57–0.61 mm). The elastic deformation at the center tends to decrease as d_P increases for 0.57 < d_P ≤ 0.60 mm, whereas the elastic deformation was separated at d_P ≥ 0.61 mm, as shown in Fig. 15 (e).

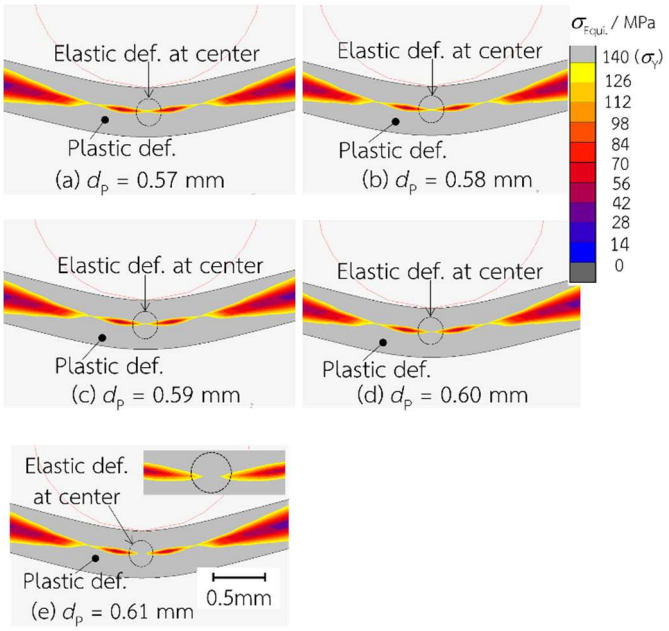

Fig. 15 Contour band diagram of equivalent stress at bending zone during the bending process of worksheet when observing the elasto-plastic state (third state). The bending profiles of the simulation results at (a) d_P = 0.57, (b) d_P = 0.58, (c) d_P = 0.59, (d) d_P = 0.60, and (e) d_P = 0.61 mm.

4.5 Effect of springback angle on simulation model

Fig. 16 shows the measurement of the springback angle S_B after unloading the bending tools of the worksheet using the simulation model. Fig. 17 shows the estimated S_B as a function of d_P for different d_P values of 0.05, 0.1, 0.5, 1.0, 1.5, and 2.0 mm, as predicted using the simulation model. To reduce the effect of S_B, a V-notch was applied to the lower side of the worksheet, as shown in Fig. 17 (ii). The ratio of the height of the V-notch (h = 0.18 mm) to the worksheet thickness (t = 0.39 mm) was approximately 2.16. The simulation results were classified into two types: (i) the simulation models were based on the experimental results, and (ii) the simulation models were modified by the V-notch on the lower side of the worksheet. The results indicate that in the case of (i), S_B tends to increase with d_P for 0.05 ≤ d_P ≤ 2.0 mm. In the case of (ii), S_B tends to increase with d_P for 0.5 ≤ d_P ≤ 2.0 mm. Conversely, in the case of (i), the characteristic of S_B appears to be higher than that in the case of (ii) for 0.05 ≤ d_P < 1.0 mm, whereas it tended to be similar in both cases for 1.0 ≤ d_P ≤ 2.0 mm, as shown in Fig. 17.

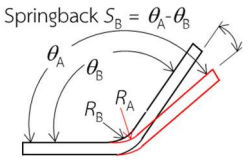

Fig. 16 Definition of springback after bending tools unloading. Here, θ_A denotes the angle after the release of the punch from bent worksheet; θ_B denotes the angle before the withdrawal of the punch at each d_P; R_A denotes the radius of curvature after the release of the punch from bent worksheet; R_B denotes the radius of curvature before the withdrawal of the punch at each d_P.

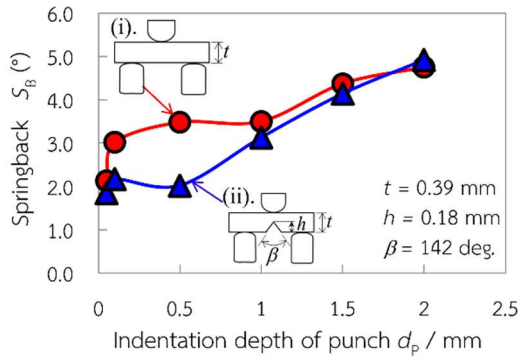

Fig. 17 Simulated springback angles after bending tool unloading. (i) Undefined V-notch (based on the experimental result) versus (ii) applied V-notch with respect to d_P states

4.6 Initial (loaded) radius of curvature of bent zone versus worksheet thickness

Fig. 18 shows the estimated radius of curvature before the withdrawal of the punch versus the worksheet thickness (R_B/t) at each d_P obtained using the simulation model. Consequently, R_B/t was varied for $0.1 \le d_P < 0.5$ mm, whereas R_B/t gradually decreased for $0.5 \le d_P \le 2.0$ mm. The ratio of $0.5 \le d_P \le 2.0$ mm to $0.1 \le d_P < 0.5$ mm was approximately 2.97:4.71.

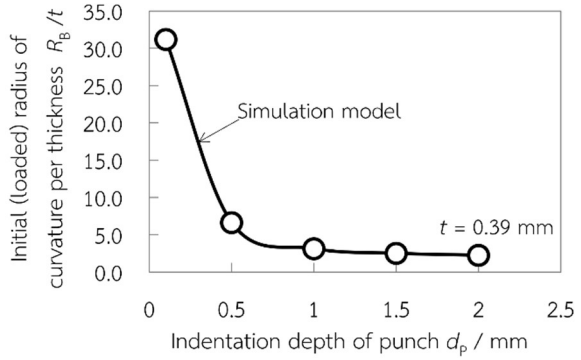

Fig. 18 Estimated initial (loaded) radius of curvature per thickness R_B/t as a function of punch indentation depth d_P

4.7 Comparison of Gardiner's model with simulation model

According to the springback of the worksheet shown in Fig. 16, Gardiner's model was used to validate the simulation results, as shown in Fig. 19. Gardiner's model was calculated using Equation (1) [8]. The springback in Gardiner's model is expressed solely by the ratio R_B/R_A. In the equation, E represents the Young's modulus of the material, σ_Y denotes yield stress, and t represents the worksheet thickness.

$$S_B = \frac{R_B}{R_A} = 4\left(\frac{R_B\sigma_y}{Et}\right)^3 - 3\left(\frac{R_B\sigma_y}{Et}\right) + 1 \quad (1)$$

Wang et al. [31]. demonstrated that the penetration of a punch with small stroke variations can significantly modify the final angle. The initial (loaded) radius of curvature R_B can be derived from the geometry of the tooling, as shown in Equation (2), where w represents the approximate half-die width, θ_B denotes the angle of curvature, d_P denotes the punch indentation depth, and $\frac{t}{2}$ denotes the worksheet thickness.

$$R_B = \frac{w\tan\theta_B + \frac{t}{2} - d_P}{\sec\theta_B - 1} \quad (2)$$

Consequently, the ratio R_B/R_A of the simulation results was higher than that of Gardiner's model for $0.1 \le d_P < 1.5$ mm. In addition, the ratio R_B/R_A of Gardiner's model was approximately 1.35–3.4 compared with that of the simulation results. However, Gardiner's model and the simulation results were similar for $1.5 \le d_P \le 2.0$ mm, as shown in Fig. 19.

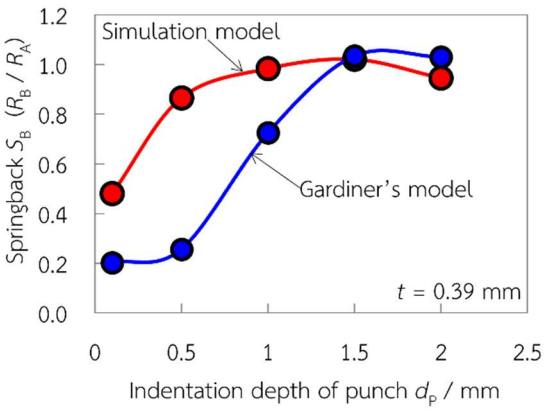

Fig. 19 Comparison between theoretical model (Gardiner's model) and simulated springback as a function of punch indentation depth d_P

5. Conclusions

The bending mechanics of a 0.39-mm-thick aluminum alloy sheet (A1050P) were evaluated experimentally and numerically using a three-point bending process. The bending characteristics of the bent part such as the bending load resistance, the effect of the kinetic friction force, the deformation profile of the bent part, σ_{P1max} (maximum principal tensile stress)/σ_{P2max} (maximum principal compressive stress), nonlinear elasto-plastic states, and springback angle states were investigated. The results are as follows:

(1). Based on the modification of the plastic coefficient in the simulation model, the plastic coefficient was assumed to be 1.89 times the original value. The modified model was confirmed by a good fit between the simulated and experimental bending forces.

(2). The contract friction force □$_c$ between the channel die and worksheet increased with the punch indentation depth d_P according to the simulation results.

(3). (3). The geometrical features at the corner of the die more significantly affected σ_{P2max} than σ_{P1max} for $0.01 < d_P \leq 2.0$ mm.

(4). The nonlinear elasto-plastic states were classified into three states. In the first state (shallow indentation cases, d_P = 0.08–0.12 mm), the elastic deformation at the center was separated for $0.12 \leq d_P \leq 0.41$ mm. In the second state (intermediate indentation cases, d_P = 0.41–0.49 mm), the recovered elastic deformation at the center tended to increase for $0.41 < d_P \leq 0.57$ mm. In the third state (deep indentation cases, d_P = 0.57–0.61 mm), the elastic deformation was separated for $d_P \geq 0.61$ mm.

(5). Comparing the springback S_B of the simulation models (based on the experimental result versus the V-notch), the simulation results of the V-notch reduced S_B in the elastic deformation state for $0.5 \leq d_P < 1.0$ mm and there were similar tendencies for the plastic deformation state when $1.0 \leq d_P \leq 2.0$ mm.

(6). R_B/t varied significantly at 24.56 for $0.1 \leq d_P \leq 0.5$ mm.

(7). The simulation and Gardiner's model showed good agreement within the specified range of $1.5 \leq d_P \leq 2.0$ mm.

Nomenclature

FEM: finite element method

d_P: indentation depth of the punch

b_F: bending force

μ_c: contract friction force

σ_{P1max}: maximum principal tensile stress

σ_{P1}: principal tensile stress

σ_{P2max}: maximum principal compressive stress

σ_{P2}: principal compressive stress

σ: tensile stress

μ_{dt}: friction coefficients between the deformable body and tools (punch and dies) It was assumed to be 0.2.

F: plastic coefficient

ε: equivalent plastic strain

n: work-hardening exponent It was 0.46 mm.

t: thickness of aluminum sheets It was 0.39 mm.

E: Young's modulus It was 78.6 GPa.

σ_Y: Yield Stress It was 140 MPa.

σ_B: Ultimate tensile strength It was 150 MPa.

L_w: length of the specimen The length was 20 mm.

W_s: width of the specimen The width was 20 mm.

S_L: span length of die The span length was 4 mm.

r_c: corner radii The corner radii was 0.6 mm.

t_p: thickness of punch The thickness of punch was 1.9 mm.

r_p: radii of punch The radii of punch was 0.95 mm.

V: experimental indentation velocity of punch It was 0.1 $mm \cdot s^{-1}$.

ϕ: punch direction angleIt was chosen as 90° with respect to the cross direction of worksheet (CD).

CD: cross direction of worksheet

μ_c: contract friction force of worksheet and tools

L_d: length of the deformable body for the simulation model The length was 20 mm.

P: pressure force

B_A: bending angle (°)

S_B: springback angle (°)

h: height of the V-notch It was 0.18 mm.

β: angle of the V-notch It was 142 deg.

θ_A: angle after the release of the punch of bent worksheet

θ_B: angle before the withdrawal the punch at each d_P

R_A: radii of curvature after the release of the punch of bent work sheet

R_B: radii of curvature before the withdrawal the punch at each d_P

Acknowledgments

This study was supported by the Nagasawa Laboratory in the Department of Mechanical Engineering at Nagaoka University of Technology, Japan, by providing the MSC. MARC software and experimental apparatus. The authors would also like to thank Professor Nagasawa Shigeru for his support during this work.

In addition, the authors are grateful to the Department of Mechanical and Manufacturing Engineering, Kasetsart University, Chalermphrakiat Sakonnakhon Province Campus, for their support throughout this study.

References

[1] Sun B, Liu R, Gu B. Numerical simulation of three-point bending fatigue of four-step 3-D braided rectangular composite under different stress levels from unit-cell approach. *Computational Materials Science*. 2012;65: 239-246.

[2] Li A, Zhao J, Wang D, Gao X, Tang H. Three-point bending fatigue behavior of WC – Co cemented

carbides. *Materials and Design*. 2013;45: 271-278.

[3] Srinivasan R, Karthik Raja G. Experimental study on bending behaviour of aluminium-copper clad sheets in V- bending process. *Mechanics & Industry*. 2019;20(6): 1-8.

[4] Bakhshivash S, Sadeghi BM, Rahimi F, Haghshenas M. Effect of bending angle and punch tip radius on spring- forward in an Al- Mg- Si Alloy. *International Mineral Processing Congress*, *11-15 Sep 2016, Quebec, Canada*. 2016. p.1-10.

[5] Ghimire S, Emeerith Y, Ghosh R, Ghosh S. Finite element analysis of an aluminium alloy sheet in a V- Die punch mechanism considering spring-back effect. *International Journal of Theoretical and Applied Mechanics*. 2017;12(2): 331-342.

[6] Maati A, Tabourot L, Balland P, Belaid S. Influence of the material microstructural properties on a 3-point bending test. *Mechanics & Industry*. 2020;21(518): 1-9.

[7] Yue Z, Qi J, Zhao X, Badreddine H, Gao J, Chu X. Springback prediction of aluminum alloy sheet under changing loading paths with consideration of the influence of kinematic hardening and ductile damage. *Metals*. 2018;8(11): 1-14.

[8] Salem C Ben, Meslameni W. A Numerical investigation on the springback in air v- bending of aluminum 1050 A. *International Journal of Research in Industrial Engineering*. 2022;11(2): 119–133.

[9] Mitsomwang P, Borrisutthekul R, Klaiw- awoot K, Pattalung A. Experimental and numerical investigations of applying tip- bottomed tool for bending advanced ultra- high strength steel sheet. *2nd International Conference on Advanced Materials Research and Manufacturing Technologies* (AMRMT 2017), *2-5 Aug 2017, Phuket, Thailand*. *Thailand:* Institute of Physics Publishing; 2017. p.1-12.

[10] Cruz DJ, Barbosa MR, Santos AD, Miranda SS, Amaral RL. Application of machine learning to bending processes and material identification. *Metals*. 2021;11(1418): 1-24.

[11] Esat V, Darendeliler H, Gokler MI. Finite element analysis of springback in bending of aluminium sheets. *Materials and Design*. 2002;23(2): 223-229.

[12] Saravanan S, Saravanan M, Jeyasimman D. Study on effects of spring back on sheet metal bending using simulation methods. *International Journal of Mechanical and Production Engineering Research and Development*. 2018;8(2): 923-932.

[13] Aday AJ. Analysis of springback behavior in steel and aluminum sheets using FEM. *Annales de Chimie - Science des Matériaux*. 2019;43(2): 95-98.

[14] Shu JS, Hung C. Finite element analysis and optimization of springback reduction: The “Double-Bend” technique. *International Journal of Machine Tools and Manufacture*. 1996;36(4): 423-434.

[15] Dizaji SA, Darendeliler H, Kaftanoğlu B. Effect of hardening models on different ductile fracture criteria in sheet metal forming. *International Journal of Material Forming*. 2016;9: 261-267.

[16] Gattmah J, Taha M, Shihab SK. Sheet metal forming processes for various materials using finite element analysis. *1st International Conference on Advances in Mechanical and Mechatronics Engineering*, *8-9 Nov 2018*, *Ankara, Turkey*. 2018. p.369-376.

[17] Kartik T, Rajesh R. Effect of punch radius and sheet thickness on spring-back in V-die bending. *Advances in Natural and Applied Sciences*. 2017;11(8): 178-183.

[18] Aljibori HSS, Hamouda AM. Finite element analysis of sheet metal forming process. *European Journal of Scientific Research*. 2009;33(1): 57-69.

[19] Thuillier S, Le Maoût N, Manach PY. Bending limit prediction of an aluminum thin sheet. *International Journal of Material Forming*. 2010;3(1): 223-226.

[20] Wagner L, Larour P, Dolzer D, Leomann F, Suppan C. Experimental issues in the instrumented 3 point bending VDA238-100 test. *International Deep- Drawing Research Group (IDDRG 2020)*, *26-30 Oct 2020*, *Seoul, South Korea*. IOP Publishing Ltd; 2020. p.1-11.

[21] Hou P, Zhao H, Ma Z, Zhang S, Li J, Dong X, et al. Influence of punch radius on elastic modulus of three- point bending tests. *Advances in Mechanical Engineering*. 2016;8(5): 1-8.

[22] Murayama M, Nagasawa S, Fukuzawa Y, Katayama I. Effect of sheet thickness and friction on load characteristic of crushed center bevel cutter indented to aluminum sheet. In: Brebbia C.A. (ed.) *Computational Methods in Contact Mechanics VI*. Southampton, England; WIT Press; 2003. p. 115-124.

[23] Murayama M, Nagasawa S, Fukuzawa Y, Katayama I. Cutting mechanism and load characteristic of trapezoidal center bevel cutter indented on aluminum sheet. *JSME International Journal, Series C: Mechanical Systems, Machine Elements and Manufacturing*. 2004;47(1): 21-28.

[24] Chaijit S, Nagasawa S, Fukuzawa Y, Murayama M, Katayama I. Effect of tip profile on cutting processability of a trapezoidal cutting blade indented to an aluminum sheet. *Journal of Mechanics of Materials and Structures*. 2006;1(8): 1301-1321.

[25] Chaijit S, Nagasawa S. FEM simulation on sensitivity of crack propagation on aluminum sheet during wedge shearing process. *Proceedings of International Conference on Leading Edge Manufacturing in 21st Century*: LEM21, *2-4 Dec 2009*, *Osaka, Japan.* The Japan Society of Mechanical Engineers: 2009. p. 379-384.

[26] Ould Ouali M, Aberkane M. Micromechanical modeling of the rolling of a A1050P aluminum sheet. *International Journal of Material Forming*. 2009;2(1): 1-18.

[27] Chakravarty P, Pál G, Bátorfi JG, Sidor JJ. Estimation of dislocation distribution at mid thickness for 1050 Al. *Acta Materialia Transylvanica*. 2022;5(1): 6-9.

[28] Jina W, Thanomputra S, Sangsuriyun M, Nagasawa S. Finite element simulation of bending process under three-point bending test of aluminum sheet. *The 4th SEITS Conference 2022 and Exhibition on Sufficiency Economy of Engineering, Innovation and Technological Development towards Leadership for Sustainability*, 5-6 Sep 2022, *Bangkok, Thailand.* Kasem Bundit University; 2022. p.66-72.

[29] ASTM International. ASTM D790-3, Standard Test Methods for Flexural Properties of Unreinforced and Reinforced Plastics and Electrical Insulating Materials, American Society for Testing and Materials. West Conshohocken; 2003.

[30] MSC Software. Marc document: *Theory and User Information*. 2014;A: p. 790-791.

[31] Wang J, Verma S, Alexander R, Gau JT. Springback control of sheet metal air bending process. *Journal of Manufacturing Processes*. 2008;10(1): 21-27.